ChemPubSoc Europe

DOI: 10.1002/chem.201704398

CHEMISTRY A European Journal Full Paper

Heterogeneous Catalysis

Activating Inert Alkali-Metal Ions by Electron Transfer from Manganese Oxide for Formaldehyde Abatement

Jiayi Gao,[a] Zhiwei Huang,[a] Yaxin Chen,[a] Jing Wan,[b] Xiao Gu,[b] Zhen Ma,[a] Jianmin Chen,[a] and Xingfu Tang*[a, c]

Abstract: Alkali-metal ions often act as promoters rather than active components due to their stable outermost electronic configurations and their inert properties in heterogeneous catalysis. Herein, inert alkali-metal ions, such as K^+ and Rb^+, are activated by electron transfer from a Hollandite-type manganese oxide (HMO) support for HCHO oxidation. Results from synchrotron X-ray diffraction, absorption, and photoelectron spectroscopies demonstrate that the electronic density of states of single alkali-metal adatoms is much higher than that of K^+ or Rb^+, because electrons transfer from manganese to the alkali-metal adatoms through bridging lattice oxygen atoms. Electron transfer originates from the interactions of alkali metal d–sp frontier orbitals with lattice oxygen sp^3 orbitals occupied by lone-pair electrons. Reaction kinetics data of HCHO oxidation reveal that the high electronic density of states of single alkali-metal adatoms is favorable for the activation of molecular oxygen. Mn L_3-edge and O K-edge soft-X-ray absorption spectra demonstrate that lattice oxygen partially gains electrons from the Mn e_g orbitals, which leads to the upshift in energy of lattice oxygen orbitals. Therefore, the facile activation of molecular oxygen by the electron-abundant alkali-metal adatoms and active lattice oxygen are responsible for the high catalytic activity in complete oxidation of HCHO. This work could assist the design of efficient and cheap catalysts by tuning the electronic states of active components.

Introduction

HCHO has been widely used in making building and furnishing materials, consumer products, and so forth. The worldwide production capacity for HCHO is over 30 million tons per year.[1] However, HCHO emitted from the above materials may cause indoor air pollution,[2] because it can lead to eye, nose, throat, and skin irritation.[3] More seriously, long-term exposure to HCHO may lead to cancer.[4,5] HCHO has been classified as a probable human carcinogen by the United States Environmental Protection Agency[6] and the World Health Organization.[3] Furthermore, HCHO is also a typical atmospheric pollutant in outdoor air,[7] because it induces photochemical pollution.[8,9] Therefore, it is of vital importance to control HCHO emissions.

Catalytic oxidation of HCHO to CO_2 and H_2O by using solid catalysts in the presence of molecular oxygen is a promising method.[10] Supported noble-metal catalysts often show excellent catalytic performance,[11–13] but they are rather expensive. Some transition-metal oxides show catalytic activity as high as that of noble-metal catalysts.[14,15] In particular, hollandite-type manganese oxides (HMO) have high catalytic activity in HCHO oxidation because the tunnel sizes are suitable for the adsorption and activation of HCHO[16] and for the activation of oxygen.[17] To further enhance the catalytic performance, noble metals such as Pt,[18] Au,[19] and Ag[20–22] were highly dispersed or even atomically dispersed/deposited onto HMO surfaces. However, noble-metal catalysts can only be applied in some special environments, such as aircraft, for cost reasons.

Occasionally, alkali metals and alkaline-earth metals, such as K^+ and Ca^{2+}, atomically dispersed and with a high electron density of states (DOS), are highly active for the catalytic oxidation of HCHO.[23,24] For instance, Han et al. found that isolated Ca^{2+} in the tunnels of hydroxyapatite showed high catalytic activity in the complete oxidation of HCHO because Ca^{2+} could activate molecular oxygen.[24] Our recent work also showed that individual K^+ of a single-site catalyst with hybridized d–sp orbitals had a high electronic DOS and possessed excellent ability to activate both molecular oxygen and lattice oxygen, and thus, the catalyst showed high catalytic activity for HCHO oxidation.[23] It should be mentioned that previous studies found that potassium exhibited promotion effects in the Fisher–Tropsch reaction[25] and ammonia synthesis,[26] and the promoting function of potassium mainly originated from

[a] J. Gao, Dr. Z. Huang, Dr. Y. Chen, Prof. Z. Ma, Prof. J. Chen, Prof. X. Tang
Institute of Atmospheric Sciences
Shanghai Key Laboratory of Atmospheric Particle Pollution and Prevention (LAP^3), Department of Environmental Science & Engineering
Fudan University, 200433 Shanghai (P.R. China)
E-mail: tangxf@fudan.edu.cn

[b] J. Wan, Prof. X. Gu
Department of Applied Physics, Chongqing University
400044 Chongqing (P.R. China)

[c] Prof. X. Tang
Jiangsu Collaborative Innovation Center of Atmospheric Environment & Equipment Technology (CICAEET)
Nanjing University of Information Science & Technology
210044 Nanjing (P.R. China)

Supporting information of this article can be found under: https://doi.org/10.1002/chem.201704398.

the electron-donating effects of potassium. Likewise, electron-abundant alkali metals can facilitate the dissociation of O_2 by charge transfer from potassium to the antibonding orbitals of O_2; thus showing significant activity in oxidation reactions.[27–29]

Herein, a series of alkali-metal ions were atomically dispersed on HMO surfaces, and the catalytic performance of these catalysts in HCHO oxidation was studied at low temperatures. The crystal structures and morphologies of the catalysts were determined by means of synchrotron X-ray diffraction (SXRD) and TEM. The specific surface areas and pore volumes of the catalysts were analyzed by N_2 adsorption–desorption measurements, and calculated by the BET and *t*-plot methods, respectively. The local structures of single alkali-metal adatoms were determined by extended X-ray absorption fine structure (EXAFS) spectra. A combination of X-ray photoelectron spectroscopy (XPS) and X-ray absorption near-edge structure (XANES) spectroscopy results revealed the electronic states and outermost orbital configuration of the isolated alkali-metal ions. Electronic interactions between Mn and O orbitals were also studied by Mn L_3-edge and O K-edge soft-X-ray absorption spectra. The catalytic performance of catalysts in HCHO oxidation is correlated with the structures and characteristics of catalysts, mainly in terms of the activation of molecular oxygen and active lattice oxygen. This work could open up an avenue to develop efficient and inexpensive single-atom catalysts for abating volatile organic compounds, such as HCHO.

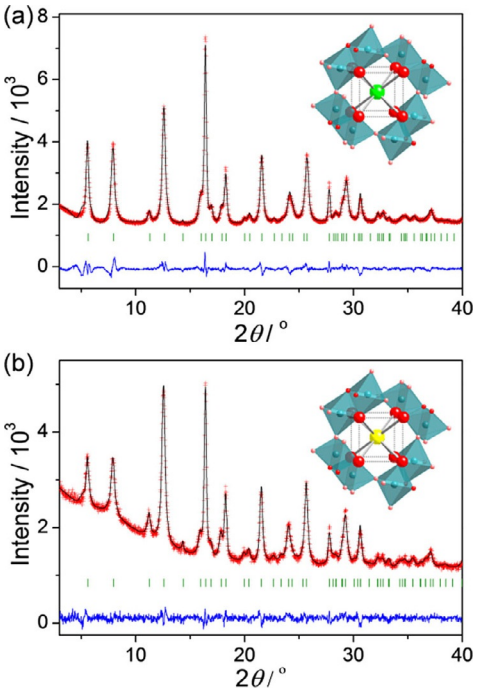

Figure 1. SXRD patterns of K_1/HMO (a) and Rb_1/HMO (b), including Rietveld refinements. The blue curves are the differential SXRD patterns. The short vertical lines below the SXRD patterns mark the peak positions of all possible Bragg reflections. Insets: oblique perspective models showing alkali-metal ions at the Wyckoff 2*b* sites. Red, blue, green, and yellow balls represent O, Mn, K, and Rb atoms, respectively; the blue octahedra represent MnO_6.

Results and Discussion

The SXRD patterns of the samples are shown in Figure 1. Rietveld refinement analyses were performed to investigate the effect of alkali-metal loading on HMO. The corresponding lattice parameters and partial atom coordinates are listed in Tables S1 and S2 in the Supporting Information, respectively, from which the structural model can be constructed (Figure 1, insets). HMO can be indexed to a tetragonal structure with the *I*4/*m* space group (Figure S1 in the Supporting Information), and thus, HMO, constructed from MnO_6 octahedra, has 1D square tunnels of about 4.7×4.7 Å^2 along the [001] direction. The tunnel walls consist of lattice oxygen with sp^3 hybridization; these lattice oxygen ions use three sp^3 orbitals to bond to three Mn^{4+}, and another sp^3 orbital occupied by lone-pair electrons can donate electrons to unoccupied orbitals of anchored metals, such as Ag and K^+.[23,30,31]

After loading the alkali metals, the tetragonal structures are preserved, regardless of the types of alkali metals, which is consistent with the results in our recent report.[32] One K or Rb ion coordinates to eight O sp^3 orbitals to form bulk-centered tetragonal prism structures, according to the results of Rietveld refinement analyses; the reconstructed models are shown in the insets of Figure 1. The K–O and Rb–O bond lengths are approximately 2.88 and 2.96 Å, respectively, which are equal to the sum of the corresponding ionic radius of alkali-metal ions and lattice oxygen.[30] The MnO_6 octahedra are also preserved after loading K or Rb. As observed in Table S1 in the Supporting Information, the lattice parameter *a* slightly increases with the atomic number of the alkali metal, and the lattice parameter *c* remains almost unchanged. Thus, the cell volume also increases upon loading of these alkali-metal ions, which is consistent with the insertion of alkali metals into the HMO tunnels in the interval stacking model because of Coulomb charge repulsion.[31] Furthermore, the specific surface areas of HMO and alkali-metal-doped HMO are in the range of 54–64 $m^2 g^{-1}$, and the pore volumes calculated from the *t*-plot method are about 1.4–2.4×10^{-3} $cm^3 g^{-1}$ (Table S3 in the Supporting Information).

The local structures of the alkali-metal atoms were investigated by EXAFS, and the related spectra at the K edge are shown in Figure 2. Tables S4 and S5 in the Supporting Information provide summaries of the structural parameters obtained by fitting the spectra with theoretical models,[31] and Figures S2 and S3 in the Supporting Information illustrate curve fitting of the *R* space and inverse FT spectra. The FT amplitudes of the EXAFS data of K_1/HMO and Rb_1/HMO are similar. The results indicate that the immediate structures of K and Rb are almost the same, that is, they are both located at the Wyckoff 2*b* sites. The first shells of K_1/HMO and Rb_1/HMO are assigned to the A–O (A = K or Rb) bonds, with average bond lengths of about 2.88 and 2.96 Å, respectively, and a coordination number of 8. Thus, a coordination configuration of an AO_8 polyhedron is D_{4h} symmetry (Figure 2, insets), as evidenced by the SXRD refinements. The results are in agreement with the conclusion reached from SXRD refinement analyses that the alkali-metal ions are arranged at an alternate stacking model along the HMO tunnel direction. Thus, the alkali-metal ions are

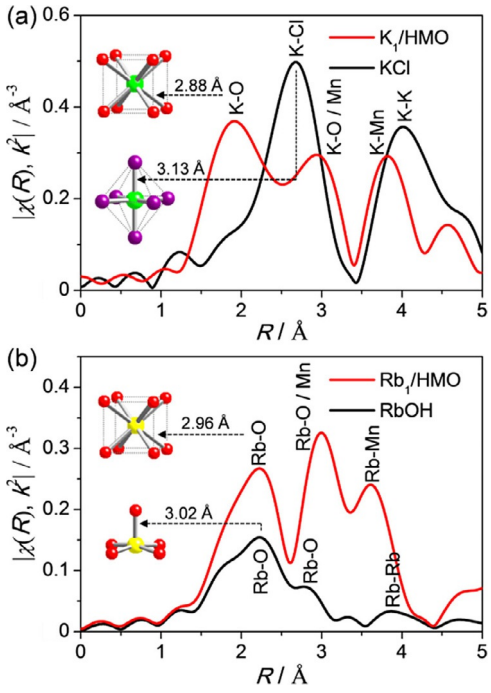

Figure 2. Fourier transform (FT) EXAFS spectra of K_1/HMO (a) and Rb_1/HMO (b) at the K and Rb K edges with k^2 weighting. Red, green, purple, and yellow balls represent O, K, Cl, and Rb atoms, respectively.

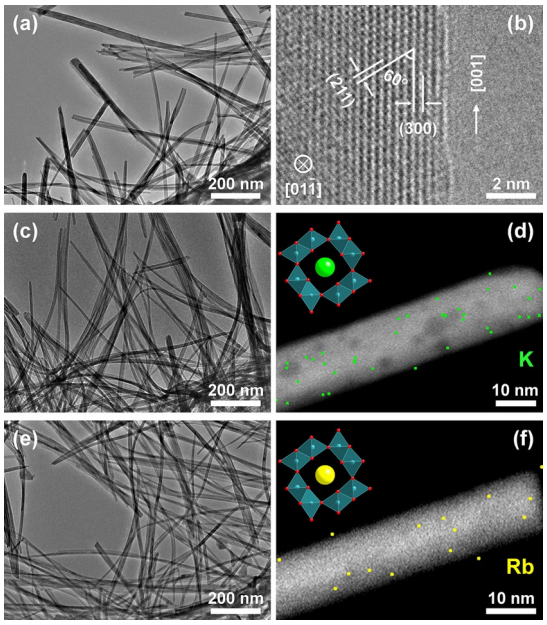

Figure 3. TEM images of HMO (a), K_1/HMO (c), and Rb_1/HMO (e). b) High-resolution (HR) TEM image of HMO. Scanning transmission electron microscopy (STEM) images, energy-dispersive X-ray spectroscopy (EDX) mapping data, and atomic arrangements on the HMO(001) planes of K_1/HMO (d) and Rb_1/HMO (f). Red, blue, green, and yellow balls represent O, Mn, K, and Rb atoms, respectively. Blue octahedra represent the MnO_6 structural motif.

located at isolated states and the single alkali-metal ions are exposed on the HMO tunnel openings to form "single-atom" alkali-metal catalysts.[23] Furthermore, the EXAFS data of the single-atom alkali-metal catalysts are distinctly different from those of KCl and RbOH. The EXAFS spectrum of KCl reveals that the local structure of K^+ is a KCl_6 octahedron, with an average K–Cl bond length of about 3.13 Å and octahedral (O_h) symmetry (Figure 2a, inset).[33] The EXAFS spectrum of RbOH reveals that the local structure of Rb^+ is a RbO_5 tetragonal pyramid, with an average Rb–O bond length of about 3.02 Å and C_{4v} symmetry (Figure 2b, inset).[34]

The morphologies of HMO, K_1/HMO, and Rb_1/HMO were observed by means of TEM. As shown in Figure 3, HMO has a rod-shaped morphology with an average length of about 800 nm and a width of about 14 nm.[32] The HMO rods grow along the [001] axis, according to the HRTEM image: 1) the fringe distances of 3.26 and 2.4 Å can be assigned to the lattice spacing of the (300) and (211) planes of HMO, respectively, and the (300) plane is parallel to the side line; and 2) the cross angle between the (211) plane and the side line is about 60°. After loading with alkali metals, the 1D morphologies of HMO remain unchanged. The appearance of smooth surfaces in the TEM images indicates the absence of KCl and RbOH nanoparticles on HMO surfaces, whereas the presence of K and Rb species is confirmed by EDX mapping data. The K/Mn or Rb/Mn molar ratios obtained from EDX analyses determine the formulas to be $K_{0.9}Mn_8O_{16}$ and $Rb_{1.0}Mn_8O_{16}$, which are in agreement with the results obtained by X-ray fluorescence spectroscopy (XRF) analyses. Consequently, the HMO tunnels are filled with alkali-metal ions, and alkali-metal ions are exposed on the HMO(001) planes, as modeled in the insets of Figure 3d and f.[23] These single alkali-metal ions are anchored on oxygen cavity sites consisting of four surface sp^3-oxygen ions.

HMO retains the same morphology and a similar structure after loading with alkali metals, which is advantageous for comparatively studying the catalytic activity of HMO and single-atom alkali-metal catalysts. The catalytic oxidation of HCHO was conducted over HMO and single-atom alkali-metal catalysts at low temperatures, and the results, in term of HCHO conversions (X_{HCHO}) and CO_2 selectivity as a function of reaction temperature, are shown in Figure 4a. All catalysts show 100% CO_2 selectivity over the whole temperature range tested. The X_{HCHO} values over HMO are significantly lower than those over the single-atom alkali-metal catalysts. K_1/HMO is slightly more active than that of Rb_1/HMO, and Rb_1/HMO has the same activity as that of Na_1/HMO prepared by using a similar method (Figure S4 in the Supporting Information). Over 95% X_{HCHO} is obtained on these single-atom alkali-metal catalysts at 110 °C, whereas HMO only gives 20% X_{HCHO} at 110 °C. The single-atom alkali-metal catalysts can even exhibit significant catalytic activities below 90 °C, but HMO is almost inactive below 90 °C, which implies that the single alkali-metal ions anchored on the HMO surfaces serve as catalytically active sites for the low-temperature oxidation of HCHO. Similar results with alkali metals as catalytic sites were also reported for the oxidation of soot and volatile organic compounds.[35,36]

The E_a value over K_1/HMO or Rb_1/HMO is about 84 kJ mol^{-1} for HCHO oxidation, which is approximately 5 kJ mol^{-1} lower than that of HMO (Figure 4b). Moreover, if Rb^+ in the form of RbOH is supported on TiO_2, RbOH/TiO_2 is inactive to HCHO oxidation (Figure S4 in the Supporting Information). Considering

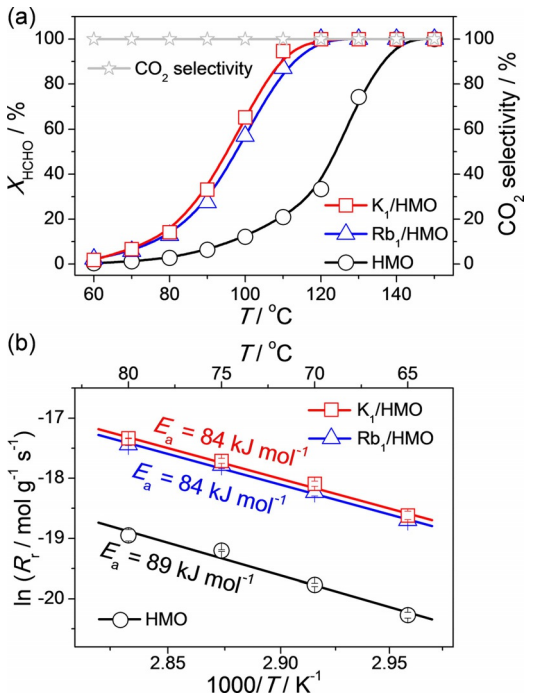

Figure 4. a) X_{HCHO} and CO_2 selectivity as a function of reaction temperature (T) over K_1/HMO, Rb_1/HMO, or HMO. b) Arrhenius plots for the reaction rates (R_r) with the corresponding activation energy (E_a) of HCHO oxidation over K_1/HMO, Rb_1/HMO, or HMO.

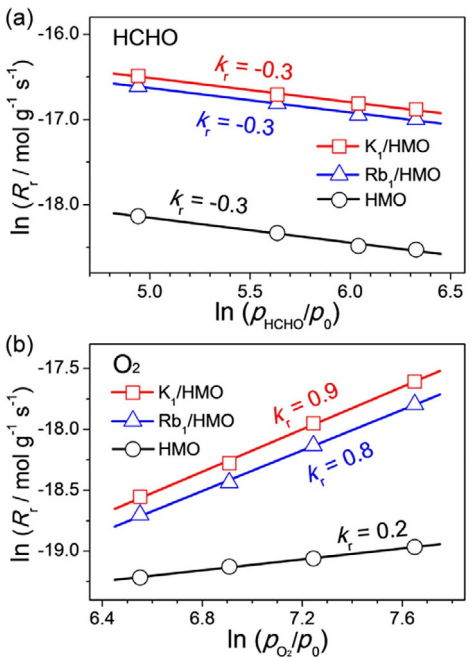

Figure 5. Reaction kinetics data for the catalytic oxidation of HCHO. Reaction orders (k_r) for HCHO (a) and O_2 (b) at a reaction temperature of 90 °C over HMO, K_1/HMO, or Rb_1/HMO.

the decrease in E_a after loading with alkali metals and the inert alkali-metal ions when loaded on TiO_2, it is convincing that the catalytic performance of the single alkali-metal adatoms on HMO is triggered by interactions among alkali metals and HMO.

The mechanism of catalytic oxidation of HCHO at low temperatures often follows the Mars–van Krevelen model,[21,37] and thus, the dissociation of O_2 and oxidation of adsorbed formate intermediate are considered to be two critical steps.[37] To identify the rate-determining step, we studied the surface reaction kinetics of HCHO oxidation at low temperatures over HMO, K_1/HMO, and Rb_1/HMO at $X_{HCHO} < 30\%$. As shown in Figure 5a, the reaction orders (k_r) of HCHO over three samples are equal ($k_r = -0.3$), which indicates that the oxidation of adsorbed formate intermediate is not the rate-determining step. The k_r value of O_2 is only 0.2 for HMO, and it dramatically increases to 0.9 for K_1/HMO and 0.8 for Rb_1/HMO (Figure 5b). Because of the negative k_r for HCHO over both HMO and the single-atom alkali-metal catalysts, the activation of O_2 will be inhibited by surface-adsorbed HCHO until surface lattice oxygen species are active enough to react with the adsorbed HCHO to produce CO_2 and H_2O, concomitant with the generation of oxygen defects. The almost first-order dependence on O_2 concentration for the single-atom alkali-metal catalysts implies that the HMO lattice oxygen species in contact with the single alkali-metal ions are highly active for converting adsorbed HCHO into CO_2 and H_2O, and that the single alkali-metal ions are very active for activating O_2. Therefore, the single-atom alkali-metal catalysts have significantly strong abilities to activate both molecular O_2 and surface lattice oxygen.

The oxygen activation of the catalysts is essentially associated with the nature of the active sites, and thus, we used X-ray absorption spectroscopy (XAS) to investigate the electronic structures of the single alkali-metal ions. Figure 6 shows the XANES data for K_1/HMO and Rb_1/HMO, together with two references at the K and Rb K edges. Because the 1s→3d pre-edge features are sensitive to the coordination geometry of excited atoms,[38] the alkali-metal ions in KCl and RbOH do not have pre-edge absorption peaks because of the 1s→3d dipole-forbidden transitions;[39] this indicates the absence of d–sp orbital hybridization, which is consistent with the stable outermost electronic configurations. In particular, the alkali-metal ions of K_1/HMO and Rb_1/HMO, with D_{4h} symmetry, have relatively intense pre-edge peaks, which indicate the presence of the 1s→3d dipole-allowed transition. The results demonstrate that the alkali-metal ions have d–sp-hybridized orbitals.[38] The alkali-metal d–sp hybridizations may originate from electron transfer from O sp^3 orbitals with lone-pair electrons to unoccupied alkali-metal d–sp frontier orbitals, resulting in electron-rich alkali-metal atoms, analogous to metallic alkali-metal atoms with the outermost hybridized orbitals.[40]

The oxidation states of the alkali-metal atoms of the single-atom alkali-metal catalysts were determined by means of K 2p and Rb 3d XPS. The electron DOS of single alkali-metal adatoms are much higher than those of ideal alkali-metal ions with a normal oxidation state of +1 in KCl or RbOH. As shown in Figure 7a, and according to our recent report,[23] it is reasonably deduced that the potassium atoms of K_1/HMO have electron DOS higher than that of K^+, and the same results are also obtained from DFT calculations (Figure S5 in the Supporting Information). Likewise, the BE of the Rb $3d_{5/2}$ peak of RbOH is centered at 109.3 eV, which is characteristic of Rb^+,[41] whereas

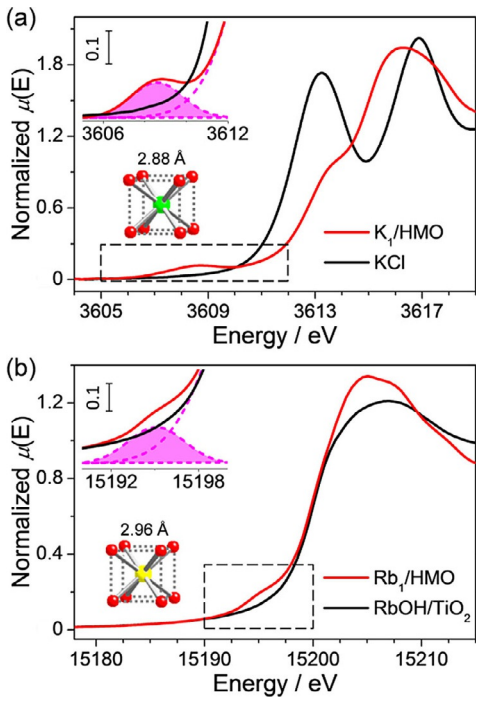

Figure 6. XANES spectra of K_1/HMO and KCl (a) and Rb_1/HMO and RbOH/TiO_2 (b) at the K and Rb K edges. Insets: spectral fitting edges, the pink shadows show the 1s→3d transition, and models of KO_8 (a) and RbO_8 (b) structural motifs.

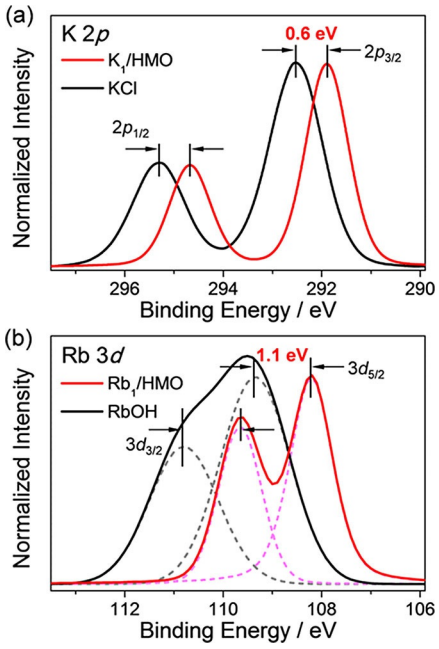

Figure 7. a) K 2p XPS results for K_1/HMO and KCl, showing the shift in binding energy (BE). b) Rb 3d XPS results for Rb_1/HMO and RbOH, showing the shift in BE.

the BE of Rb $3d_{5/2}$ of Rb_1/HMO decreases to about 108.2 eV through a downshift of about 1.1 eV with respect to that of RbOH (Figure 7b), indicative of the high electronic DOS of Rb ions. The results are in line with the above XANES data. The single alkali-metal adatoms, with hybridized d–sp orbitals and high electronic DOS, are energetically favorable for the adsorption and subsequent dissociation of O_2: 1) orbital hybridization of single alkali-metal adatoms by local transfer of sp electrons to an empty d shell allows O_2 to approach alkali-metal atoms until chemisorption occurs because of weakening of the Pauli repulsion; and 2) abundant electrons of single alkali-metal adatoms are favorable for charge transfer to antibonding π* orbitals of O_2 to weaken the O–O bond until dissociation occurs.[27] As a consequence, the high electronic DOS of the single alkali-metal adatoms is mainly responsible for the strong ability towards activating O_2.

The activation of oxygen also includes the activation of lattice oxygen, as well as molecular O_2. Figure 8 depicts the O 1s XPS results for HMO and K_1/HMO and Rb_1/HMO, together with their differences. Clearly, the O 1s XPS results for K_1/HMO and

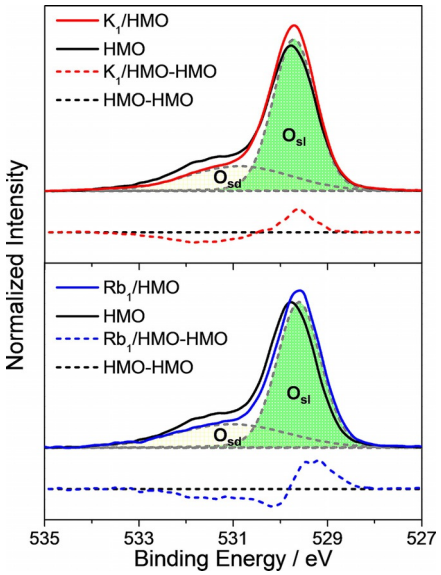

Figure 8. O 1s XPS results for HMO and K_1/HMO and Rb_1/HMO, together with their differences (dotted lines). The shades in different colors show curve-fitting results, and the shades in yellow and green represent O_{sd} and O_{sl} species, respectively.

Rb_1/HMO slightly shift to lower BE relative to those of HMO, which illustrates that the O species gain electrons after the loading of alkali metals on HMO. The main peak in the BE range of 529.6–529.8 eV is assigned to surface lattice oxygen (O_{sl}) species of HMO, and the smaller shoulder in a BE range of 530.9–531.3 eV is ascribed to surface defect oxygen (O_{sd}) species of HMO.[42] In particular, the O_{sd} species decrease, while the O_{sl} species increase in single-atom alkali-metal catalysts, with respect to those of HMO; this implies that the concentration of O_{sl} species of HMO increases after the loading of alkali metals. On the basis of the Mars–van Krevelen model, the O_{sl} species are of great importance for low-temperature oxidation of HCHO because O_{sl} with nucleophilic properties can attack the electrophilic carbonyl group of HCHO readily.[43] Therefore, the enhancement of the concentration of O_{sl} species upon loading with alkali metals could partially account for the activity improvement of K_1/HMO and Rb_1/HMO. Therefore, according

to the evidence and related discussion, the enhancement of the single-atom alkali-metal catalysts mainly originates from the facile activation of molecular O_2 by electron-abundant alkali-metal ions and active lattice oxygen due to the alkali-metal loading.

The significant change in the catalytic performance of inert alkali-metal ions when they are loaded on HMO may essentially originate from electronic metal–support interactions (EMSI). Thus, we recorded soft-X-ray adsorption spectra of the samples to shed light on such interactions. According to DFT calculations and previous reports,[44,45] the insulating HMO will become conducting after alkali metals are inserted into the tunnels. Because the electronegativity of manganese is much smaller than that of oxygen, electrons transferred to alkali metals should mainly originate from manganese. Accordingly, we studied changes to the Mn L_3-edge soft-X-ray absorption spectra of HMO after the insertion of K ions into the tunnels (Figure 9a).

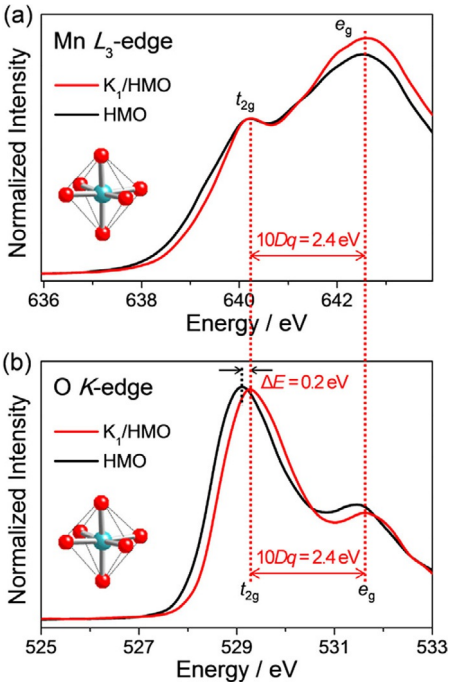

Figure 9. a) Mn L_3 and b) O K-edge soft-X-ray absorption spectra of HMO and K_1/HMO. Inset: MnO_6 octahedron. Red and blue balls represent O and Mn, respectively.

According to the O_h symmetry of Mn and crystal field theory, two peaks in the Mn L_3-edge soft-X-ray absorption spectra of HMO and K_1/HMO are assigned to the $2p_{3/2} \rightarrow t_{2g}$ and $2p_{3/2} \rightarrow e_g$ transitions, and thus, an energy difference between t_{2g} and e_g orbitals, an octahedral ligand-field splitting parameter, $10Dq$, is calculated to be about 2.4 eV, which is consistent with the reported value.[46] In particular, the intensity of the peak due to the $2p_{3/2} \rightarrow e_g$ transition is slightly stronger for K_1/HMO than that for HMO; thus the unoccupied states increase for K_1/HMO, that is, Mn partially loses e_g electrons after K insertion because pristine HMO has a minority of Mn^{3+} with $3d^4$ electrons in a high-spin electron configuration, $t_{2g}^3 e_g^1$.[47] Possibly, electron transfer from Mn to K through the bridging oxygen of K–O–Mn occurs if K ions are inserted into HMO tunnels.

To substantiate the above hypothesis, we recorded the O K-edge soft-X-ray adsorption spectra of HMO and K_1/HMO. As shown in Figure 9b, a distinct feature of two peaks with an energy difference of about 2.4 eV provides evidence that the O 2p orbitals have hybridized with the Mn 3d orbitals.[46] The high-energy peak intensity of K_1/HMO with the "e_g" feature is slightly weaker with respect to that of HMO, which indicates that the occupied states of the O 2p orbitals with the e_g feature increase. By comparing the peak intensity due to the Mn e_g orbitals with the intensity of the O 2p orbitals with the e_g feature, we conclude that electrons from the Mn e_g orbitals have transferred into the unoccupied O 2p orbitals through hybridization. Therefore, electron transfer from manganese to alkali metals through bridging oxygen allows alkali metals to be at high electronic DOS.

In Figure 9b, another important characteristic of the O K-edge soft-X-ray absorption spectra is the upshifted spectrum of K_1/HMO with respect to that of HMO, which indicates that electron transfer from the Mn e_g orbitals to the unoccupied O 2p orbitals leads to the shift of the electronic states of O to a higher energy (by 0.2 eV in comparison with that of HMO). As discussed above, the electronic DOS of the high-energy O 2p orbitals with the e_g feature increase due to the insertion of K^+ into HMO tunnels. Hence, the upshifted O 2p orbitals with the high electronic DOS should improve the redox ability of single-atom alkali-metal catalysts, which possibly accounts for the production of the highly active lattice oxygen after loading with alkali metals.

Figure 10 shows the H_2 temperature-programmed reduction (H_2-TPR) profiles of HMO and K_1/HMO. As shown in Figure 10a, HMO exhibits three reduction peaks. The first and second peaks are located at about 269 and 279 °C, respectively, whereas the third weak, broad peak starts at 300 °C with a maximum at about 445 °C. The area ratio of H_2 consumption (A_{H_2}) between the sum of the first two peaks and the third peak is about 1.6:1, from which the oxidation state of Mn can be calculated to be about 3.7; this indicates the presence of Mn^{3+} and Mn^{4+}, and thus, the formula of HMO can be simplified to $MnO_{1.9}$. The first peak is due to the reduction of surface oxygen (O_{sd} and O_{sl}) species. The second and third peaks can be assigned to the reduction of the bulk lattice oxygen (O_{bl}) species, that is, the reduction of $MnO_{1.9}$ to Mn_3O_4, and the reduction of Mn_3O_4 to MnO.[16] After alkali-metal loading, two typical features of the H_2-TPR profile of K_1/HMO can be observed: 1) the surface O species increase, and 2) the temperature required for the reduction of the O_{bl} species shifts to the low-temperature window.

To shed light on the discrepancy after alkali-metal loading, the difference curves were obtained by subtracting the H_2-TPR curve of HMO (Figure 10b), and thus, a peak centered at about 230 °C could be attributed to the reduction of O_{sl} at the vicinity of alkali-metal ions; this indicates that the number of active O_{sl} increases and the redox ability is improved, which is consistent with the upshift in energy of the O K-edge soft-X-ray absorp-

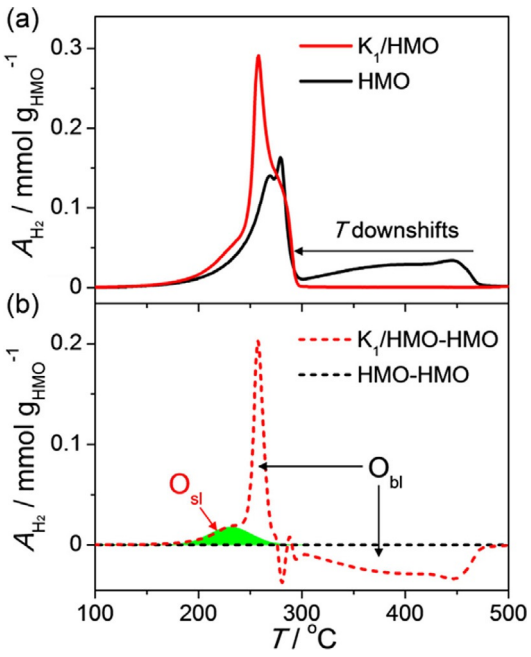

Figure 10. a) H_2-TPR profiles of HMO and K_1/HMO, and b) difference curves obtained by subtracting the H_2-TPR curve of HMO. The green shade in panel b) represents H_2 consumption by active O_{sl} at the vicinity of alkali-metal ions.

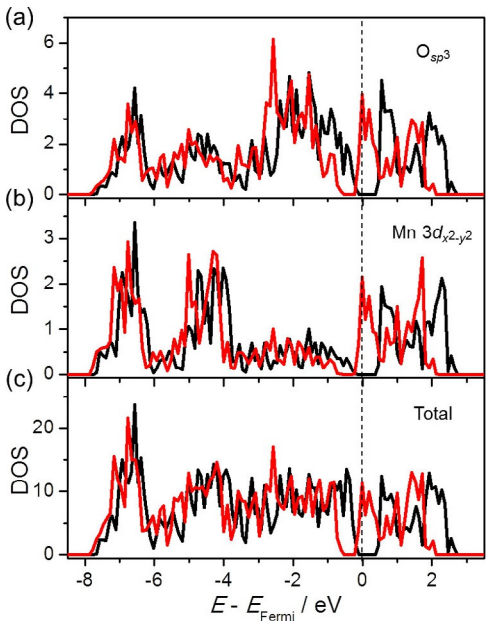

Figure 11. DOS of the O_{sp^3} (a) and Mn $3d_{x^2-y^2}$ (b) orbitals of HMO (black) and K_1/HMO (red). c) Total DOS of HMO (black) and K_1/HMO (red).

tion spectra of K_1/HMO in Figure 9b. Moreover, the abundance of active O_{sl} species is also favorable for improving the catalytic activity in HCHO oxidation. Notably, after alkali-metal loading, the high-temperature reduction peak of HMO drastically shifts to the low-temperature range, and the peaks due to the reduction of O_{sl} fall into a narrow temperature window, which implies that alkali-metal loading accelerates the transfer rates of electrons produced in the redox reaction of H_2 with O_{bl}. Therefore, electron transfer between alkali metals and HMO enhances the redox ability; thus leading to the high catalytic activity of the single-atom alkali-metal catalysts in HCHO oxidation.

To investigate the EMSI in detail, we carried out DFT calculations based on HMO and K_1/HMO. Figure 11a and b depicts the electronic DOS of HMO and K_1/HMO. The DOS of the O_{sp^3} orbital bound to K^+ shifts downward in energy, with respect to that of HMO, which makes the DOS of Mn $3d_{x^2-y^2}$ orbitals shift down below the Fermi level (E_{Fermi}). The DOS downshifts of both O and Mn demonstrate that strong EMSI occurs along the K–O–Mn structural motif. These results agree with the soft-X-ray absorption spectroscopy results in Figure 9, and proves electron transfer from Mn to K through the bridging O. Figure 11c shows the total DOS of HMO and K_1/HMO. Interestingly, the EMSI induces an insulator-to-conductor transition (HMO is insulating, but K_1/HMO is conducting), which is favorable for facilitating electron transfer in catalytic reactions; thus leading to enhanced redox ability (Figure 10) and catalytic activity (Figure 4).[27] Likewise, alkaline-earth-metal ions, such as Ca^{2+}, were able to improve the oxidizing ability of manganese–oxido clusters[48] or iron–oxo complexes[49] by accelerating electron transfer in oxidation reactions. Therefore, the EMSI allows the DOS of the alkali-metal ions to increase through electron transfer from Mn to K, which improves the activation of O_2 and lattice oxygen; thus leading to high catalytic activity in HCHO oxidation.

Conclusions

Single-atom alkali-metal catalysts were synthesized by anchoring individual alkali-metal atoms on the tunnel openings of HMO. The structures were precisely determined by means of SXRD, X-ray absorption, and TEM. These single-atom alkali-metal catalysts exhibited high catalytic activity in the complete oxidation of HCHO in the presence of O_2 at low temperatures. The characterization results demonstrated that the single alkali-metal atoms had hybridized frontier d–sp orbitals through strong interactions with lattice oxygen, and that electron transfer from the Mn e_g orbitals to the alkali-metal d–sp hybridized orbitals through the alkali-metal–O–Mn bridging O resulted in alkali-metal atoms with high electronic DOS. Hence, electron-rich alkali-metal atoms with hybridized orbitals could facilitate the adhesion and activation of O_2. The combination of O K-edge soft-X-ray absorption spectra and H_2-TPR profiles revealed that the electronic states of the single-atom alkali-metal catalysts shifted up in energy, so that the lattice oxygen showed strong redox ability. Therefore, the high electron DOS of the single alkali-metal atoms and high activity of lattice oxygen were responsible for the high catalytic activity of the single-atom alkali-metal catalysts in HCHO oxidation.

Experimental Section

Catalyst preparation

HMO was prepared by a refluxing route:[32] $MnSO_4{\cdot}H_2O$ (25.350 g, 0.15 mol), $(NH_4)_2S_2O_8$ (34.200 g, 0.15 mol), and $(NH_4)_2SO_4$ (99.000 g,

0.75 mol) were dissolved in deionized water (0.4 L) to give an aqueous solution. Then the solution was heated for 12 h at reflux. The resulting slurry was filtered, washed with deionized water, dried at 110 °C for 12 h, and the obtained black solid was calcined in air at 400 °C for 4 h.

Single-atom alkali-metal catalysts were prepared by an impregnation method. In a typical synthesis, KCl (0.216 g, 2.9 mmol) or RbOH (0.297 g, 2.9 mmol) was added to a suspension (50 mL) containing HMO (2.000 g, 23.0 mmol) under vigorous stirring for 15 min. Then the suspension was transferred to a rotary evaporator and the temperature was kept at 80 °C to remove excess water. The obtained dry samples were labeled as KCl/HMO and RbOH/HMO, respectively. The A_1/HMO (A = K or Rb) sample was obtained after annealing KCl/HMO or RbOH/HMO at 400 °C for 12 h and the final powder was washed with deionized water at room temperature. The alkali-metal loadings (4.8 wt% for K_1/HMO and 10.4 wt% for Rb_1/HMO) were determined by means of XRF on a Bruker-AXS S4 Explorer instrument. For comparison, RbOH/TiO_2 was also prepared by impregnation of TiO_2 (2.000 g, 25.0 mmol) with RbOH (0.297 g, 2.9 mmol) and without further annealing.

Catalyst characterization

SXRD was performed at BL14B of the Shanghai Synchrotron Radiation Facility (SSRF) at a wavelength of 0.6887 Å. Rietveld refinements of the diffraction data were performed with the FULLPROF software package on the basis of the *I4/m* space group.

The specific surface area and pore volume were analyzed on a Micromeritics Tristar II 3020 surface area and pore size analyzer by N_2 adsorption–desorption measurements at −196 °C, and calculated by the BET and *t*-plot methods, respectively.

XAS results for K_1/HMO, including XANES and EXAFS data at the K K-edge, were collected at BL4B7A of the Beijing Synchrotron Radiation Facility (BSRF). The Rb K-edge XANES and EXAFS data were collected at BL14W of the SSRF. The raw data were analyzed by using the IFEFFIT 1.2.11 software package. The soft-X-ray absorption spectra at the Mn L edge and O K edge were obtained in total electron yield (TEY) mode at BL08U1A of the SSRF.

TEM and HRTEM images were obtained on a JEM 2100F transmission electron microscope with an EDX attachment for the determination of elemental contents.

XPS results were obtained on a Kratos Axis Ultra-DLD system with a charge neutralizer and a 150 W Al (Mono) X-ray gun (1486.6 eV). The samples were dried in vacuum before XPS analysis. XPS results were referenced to the C 1s peak at a BE of 284.6 eV. Data analysis and processing were undertaken by using XPSPeak 4.1 software with the Shirley-type background.

The H_2-TPR profiles were measured by using a thermal conductivity detector (TCD) on a Micromeritics 2720 adsorption instrument (Micromeritics, USA). A sample (50 mg) was loaded and reduced with 10.0 vol% H_2/Ar (50 mL min^{-1}) at a heating rate of 10 °C min^{-1}. The A_{H_2} values were calculated and calibrated by using pure CuO samples.

Catalytic evaluations

The catalytic oxidation of HCHO was conducted in a fixed-bed quartz reactor (inner diameter = 8 mm) at atmospheric pressure. A fresh catalyst (50 mg, 40–60 mesh) was loaded for each run. Gaseous HCHO was generated by passing N_2 over paraformaldehyde (96%, Acros) in a container, which was immersed in a water bath to keep the temperature at 45 °C. The HCHO/N_2 gas was mixed with another O_2 flow to give a total gas stream of 140 ppm HCHO/10.0 vol% O_2/N_2 (100 mL min^{-1}). The gas hourly space velocity was 60 000 h^{-1}. Gas analysis was undertaken by using an online Agilent 7890A gas chromatograph equipped with a TCD. The CO_2 selectivity was correctly measured by using an online Agilent 7890B gas chromatograph equipped with a flame ionization detector (FID) and Ni catalyst converter, which could convert carbon oxides quantitatively into methane in the presence of H_2 before the detector. No other carbon-containing compounds, except CO_2, were detected in the effluents for the whole tested temperature window and all tested catalysts. The kinetics of HCHO oxidation was studied at 90 °C over K_1/HMO, Rb_1/HMO, and HMOby controlling $X_{HCHO} < 30\%$ as well as excluding external and internal diffusion to achieve data of the intrinsic reaction kinetics. The HCHO concentration ranged from 140 to 560 ppm, and the corresponding O_2 concentration ranged from 700 to 2100 ppm. In typical runs, the data were recorded at the steady state.

Theoretical calculations

All of the features were based on DFT as implemented in the Vienna ab initio simulation package (VASP). The local density approximation (LDA) for the exchange and correlation effects was used in the calculations. To describe interactions between the core and valence electrons, the pseudopotentials of the projector augmented wave method were used. The plane wave energy was equal to 500 eV, and a 2×2×6 Monkhorst–Pack grid was used for *k*-space sampling in the calculation of HMO or K_1/HMO. For the geometry optimization, the force and energy cutoff were set as 0.01 eV Å^{-1} and 10^{-6} eV, respectively. The lattice constants and Wyckoff site information for a conventional tetragonal cell are listed in Tables S1 and S2 in the Supporting Information. A supercell containing eight formula units of MnO_2 was employed in the calculations for K^+ in the terminal tunnels. For the DOS calculations of the system, we used LDA with the Hubbard U corrections (LDA + U) method, and the *U* and *J* values were set as 5.6 and 1.0 eV, respectively.[50,51]

Acknowledgements

This work was financially supported by the NSFC (21477023 and 21777030). The SXRD and XAS measurements were conducted at the SSRF and BSRF, Chinese Academy of Sciences.

Conflict of Interest

The authors declare no conflict of interest.

Keywords: alkali metals · electron transfer · heterogeneous catalysis · structure elucidation · oxygen activation

[1] X. Tang, Y. Bai, A. Duong, M. T. Smith, L. Li, L. Zhang, *Environ. Int.* **2009**, *35*, 1210 – 1224.
[2] O. Wittmann, *Eur. J. Wood Wood Prod.* **1962**, *20*, 221 – 224.
[3] *WHO Guidelines for Indoor Air Quality: Selected Pollutants*, World Health Organization Regional Office for Europe, Copenhagen, Denmark, **2010**.
[4] W. D. Kerns, K. L. Pavkov, D. J. Donofrio, E. J. Gralla, J. A. Swenberg, *Cancer Res.* **1983**, *43*, 4382 – 4392.
[5] J. A. Swenberg, W. D. Kerns, R. I. Mitchell, E. J. Gralla, K. L. Pavkov, *Cancer Res.* **1980**, *40*, 3398 – 3402.
[6] *Integrated Risk Information System (IRIS): Formaldehyde*, US Environmental Protection Agency, **2006**.

[7] T. Salthammer, *Angew. Chem. Int. Ed.* **2013**, *52*, 3320 – 3327; *Angew. Chem.* **2013**, *125*, 3402 – 3410.
[8] Y. Kuwabara, G. V. Alexeeff, R. Broadwin, A. G. Salmon, *Environ. Health Perspect.* **2007**, *115*, 1609 – 1616.
[9] J. P. Pinto, G. R. Gladstone, Y. L. Yung, *Science* **1980**, *210*, 183 – 184.
[10] J. Q. Torres, S. Royer, J. P. Bellat, J. M. Giraudon, J. F. Lamonier, *ChemSusChem* **2013**, *6*, 578 – 592.
[11] X. Tang, J. Chen, X. Huang, Y. Xu, W. Shen, *Appl. Catal. B: Environ.* **2008**, *81*, 115 – 121.
[12] L. Ma, D. Wang, J. Li, B. Bai, L. Fu, Y. Li, *Appl. Catal. B: Environ.* **2014**, *148 – 149*, 36 – 43.
[13] D. W. Kwon, P. W. Seo, G. J. Kim, S. C. Hong, *Appl. Catal. B: Environ.* **2015**, *163*, 436 – 443.
[14] J. Wang, J. Li, C. Jiang, P. Zhou, P. Zhang, J Yu, *Appl. Catal. B: Environ.* **2017**, *204*, 147 – 155.
[15] J. Zhou, L. Qin, W. Xiao, C. Zeng, N. Li, T. Lv, H. Zhu, *Appl. Catal. B: Environ.* **2017**, *207*, 233 – 243.
[16] T. Chen, H. Dou, X. Li, X. Tang, J. Li, J. Hao, *Micropor. Mesopor. Mater.* **2009**, *122*, 270 – 274.
[17] S. Liang, F. Teng, G. Bulgan, R. Zong, Y. Zhu, *J. Phys. Chem. C* **2008**, *112*, 5307 – 5315.
[18] X. Yu, J. He, D. Wang, Y. Hu, H. Tian, Z. He, *J. Phys. Chem. C* **2012**, *116*, 851 – 860.
[19] X. Yu, J. He, D. Wang, Y. Hu, H. Tian, T. Dong, Z. He, *J. Nanopart. Res.* **2012**, *14*, 1260.
[20] H. Tian, J. He, L. Liu, D. Wang, *Ceram. Int.* **2013**, *39*, 315 – 321.
[21] Z. Huang, X. Gu, Q. Cao, P. Hu, J. Hao, J. Li, X. Tang, *Angew. Chem. Int. Ed.* **2012**, *51*, 4198 – 4203; *Angew. Chem.* **2012**, *124*, 4274 – 4279.
[22] P. Hu, Z. Amghouz, Z. Huang, F. Xu, Y. Chen, X. Tang, *Environ. Sci. Technol.* **2015**, *49*, 2384 – 2390.
[23] F. Xu, Z. Huang, P. Hu, Y. Chen, L. Zheng, J. Gao, X. Tang, *Chem. Commun.* **2015**, *51*, 9888 – 9891.
[24] J. Xu, T. White, P. Li, C. He, Y. F. Han, *J. Am. Chem. Soc.* **2010**, *132*, 13172 – 13173.
[25] D. J. Dwyer, J. H. Hardenbergh, *Appl. Surf. Sci.* **1984**, *19*, 14 – 27.
[26] G. Ertl, M. Weiss, S. B. Lee, *Chem. Phys. Lett.* **1979**, *60*, 391 – 394.
[27] C. Janiak, R. Hoffmann, P. Sjövall, B. Kasemo, *Langmuir* **1993**, *9*, 3427 – 3440.
[28] J. Harris, S. Andersson, *Phys. Rev. Lett.* **1985**, *55*, 1583 – 1586.
[29] J. E. Post, R. B. Von Dreele, P. R. Buseck, *Acta Crystallogr. B* **1982**, *38*, 1056 – 1065.
[30] R. D. Shannon, C. T. Prewitt, *Acta Crystallogr. B* **1969**, *25*, 925 – 946.
[31] J. Vicat, E. Fanchon, P. Strobel, D. Tran Qui, *Acta Crystallogr. B* **1986**, *42*, 162 – 167.
[32] P. Hu, M. E. Schuster, Z. Huang, F. Xu, S. Jin, Y. Chen, W. Hua, D. S. Su, X. Tang, *Chem. Eur. J.* **2015**, *21*, 9619 – 9623.
[33] J. Vogt, H. Weiss, *Surf. Sci.* **2001**, *491*, 155 – 168.
[34] S. Odde, H. M. Lee, M. Kołaski, B. J. Mhin, K. S. Kim, *J. Chem. Phys.* **2004**, *121*, 4665 – 4670.
[35] Q. Li, X. Wang, Y. Xin, Z. Zhang, Y. Zhang, C. Hao, M. Meng, L. Zheng, L. Zheng, *Sci. Rep.* **2014**, *4*, 4725.
[36] Y. Chen, G. Tian, M. Zhou, Z. Huang, C. Lu, P. Hu, J. Gao, Z. Zhang, X. Tang, *Environ. Sci. Technol.* **2016**, *50*, 5825 – 5831.
[37] C. F. Mao, M. A. Vannice, *J. Catal.* **1995**, *154*, 230 – 244.
[38] S. Bordiga, E. Groppo, G. Agostini, J. A. van Bokhoven, C. Lamberti, *Chem. Rev.* **2013**, *113*, 1736 – 1850.
[39] L. G. Parratt, *Rev. Mod. Phys.* **1959**, *31*, 616 – 645.
[40] L. Pauling, *General Chemistry*, BN Publishing, **2011**.
[41] R. Itti, I. Tomeno, K. Ikeda, K. Tai, N. Koshizuka, S. Tanaka, *Phys. Rev. B* **1991**, *43*, 435 – 440.
[42] Q. Tang, L. Jiang, J. Liu, S. Wang, G. Sun, *ACS Catal.* **2014**, *4*, 457 – 463.
[43] X. Tang, J. Chen, Y. Li, Y. Xu, W. Shen, *Chem. Eng. J.* **2006**, *118*, 119 – 125.
[44] M. Toupin, T. Brousse, D. Bélanger, *Chem. Mater.* **2004**, *16*, 3184 – 3190.
[45] W. Xiao, H. Xia, J. Y. Fuh, L. Lu, *J. Power Sources* **2009**, *193*, 935 – 938.
[46] M. Abbate, F. M. F. de Groot, J. C. Fuggle, A. Fujimori, O. Strebel, F. Lopez, M. Domke, G. Kaindl, G. A. Sawatzky, M. Takano, Y. Takeda, H. Eisaki, S. Uchida, *Phys. Rev. B* **1992**, *46*, 4511 – 4519.
[47] P. Umek, A. Gloter, M. Pregelj, R. Dominko, M. Jagodič, Z. Jagličić, A. Zimina, M. Brzhezinskaya, A. Potočnik, C. Filipič, A. Levstik, D. Arčon, *J. Phys. Chem. C* **2009**, *113*, 14798 – 14803.
[48] E. Y. Tsui, R. Tran, J. Yano, T. Agapie, *Nature Chem.* **2013**, *5*, 293 – 299.
[49] Y. Morimoto, H. Kotani, J. Park, Y. Lee, W. Nam, S. Fukuzumi, *J. Am. Chem. Soc.* **2011**, *133*, 403 – 405.
[50] F. Zhou, M. Cococcioni, C. A. Marianetti, D. Morgan, G. Ceder, *Phys. Rev. B* **2004**, *70*, 235121.
[51] D. A. Tompsett, M. S. Islam, *Chem. Mater.* **2013**, *25*, 2515 – 2526.

Manuscript received: September 19, 2017
Accepted manuscript online: October 14, 2017
Version of record online: December 13, 2017